Toward real-time shear-wave imaging
Ultradense magnetic sources enable rapid diffuse field correlations

Laloy-Borgna, G.; Giammarinaro, B.; Sun, Z.; Catheline, S.; Aichele, J.

DOI
10.1103/PhysRevApplied.22.064061

Publication date
2024

Document Version
Final published version

Published in
Physical Review Applied

Citation (APA)
Laloy-Borgna, G., Giammarinaro, B., Sun, Z., Catheline, S., & Aichele, J. (2024). Toward real-time shear-wave imaging: Ultradense magnetic sources enable rapid diffuse field correlations. *Physical Review Applied*, *22*(6), Article 064061. https://doi.org/10.1103/PhysRevApplied.22.064061

PHYSICAL REVIEW APPLIED **22,** 064061 (2024)

Toward real-time shear-wave imaging: Ultradense magnetic sources enable rapid diffuse field correlations

G. Laloy-Borgna,[1,2] B. Giammarinaro,[1,*] Z. Sun,[3] S. Catheline,[1] and J. Aichele[1,4,†]

[1] *LabTAU, INSERM, Centre Léon Bérard, Université Claude Bernard Lyon 1, F-69003, Lyon, France*
[2] *Department of Imaging Physics, Delft University of Technology, Delft 2628 CJ, The Netherlands*
[3] *College of Information and Communication Engineering, Faculty of Information Technology, Beijing University of Technology, Beijing, China*
[4] *Department of Earth Sciences, Institute of Geophysics, Swiss Federal Institute of Technology, Zürich, Switzerland*

(Received 31 August 2023; revised 24 November 2024; accepted 26 November 2024; published 17 December 2024)

Perfectly diffuse wave fields are the underlying assumption for noise-correlation tomography in seismology, nondestructive testing, and elastography; however, perfectly diffuse fields are rarely encountered in real-world applications. We show that homogeneously distributed magnetic microparticles allow instantaneous generation of a diffuse wave field, which can be imaged using a clinical probe connected to a fully programmable ultrasound scanner. The particles are placed inside a bilayered hydrogel and act as elastic-wave sources on excitation by a magnetic pulse. Using ultrafast ultrasound imaging coupled to phase tracking, the diffuse elastic wave field is imaged. This allows the local wave velocity to be measured everywhere on the image using noise-correlation algorithms inspired by seismology. Thanks to this instantaneous diffuse wave field, a very short acquisition time is sufficient to retrieve the wave speed contrast of a bilayered phantom. The correlation time window can be shrunk down to three time samples, which we show in a numerical simulation mimicking the experimental conditions. Our experimental and numerical results are consistent with theoretical predictions made by information theory, and they pave the way for real-time elasticity imaging. This is of particular interest for monitoring of medical treatments through real-time tissue-elasticity assessment, and it is also applicable in related fields such as seismology and nondestructive testing.

DOI: 10.1103/PhysRevApplied.22.064061

I. INTRODUCTION

Passive imaging methods are based on the extraction of information from random wave fields naturally occurring within a body of interest. This enables imaging without the need for precisely controlled sources by exploiting rather than suppressing what is commonly called “noise.” In the context of elastic waves, passive imaging methods are widely applied in global and environmental seismology, seismic exploration, nondestructive testing, and medical imaging. Examples include seismic interferometry [1,2], noise or coda correlation for earthquakes [3] and icequakes [4], synthetic wave Lamb focusing in nondestructive testing [5], and passive seismic tomography [6] for reservoir monitoring. In medical imaging for tissue-stiffness estimation, passive elastography exploits the shear-wave fields naturally present in the human body, retrieving a shear-wave speed map from the correlation of ultrasound (US) [7,8], magnetic resonance imaging (MRI) [9], or optical imaging [10,11]. The imaged shear-wave field commonly results from cardiac activity, arterial pulsatility, or muscle activity. A comprehensive review of different passive elastography algorithms was published recently [12].

Extracting information from noise through cross-correlation is closely related to time reversal [13]; it relies on source-receiver reciprocity [14] to retrieve the exact impulse response or Green’s function between two points. This method is based on the assumption that the wave field is diffuse, which means that at each location and frequency, it is an “isotropic random superposition of plane waves” [15]. This is achieved through homogeneous source distribution or multiple scattering. The first experimental proof of this employed scattered thermal fluctuations from ultrasonic fields in an aluminium cylinder [16]. Homogeneous source distributions are rarely considered due to difficulties in experimental realization [17] and issues arising when sources inside the region of interest contribute [18,19]. Experimental realization of homogeneous source distributions is facilitated when the sources can be activated remotely, as is the case with magnetic particles.

---

[*] Contact author: bruno.giammarinaro@inserm.fr
[†] Contact author: johannes.aichele@rwth-aachen.de

Biocompatible magnetic nanoparticles are widely used as contrast agents in magnetic resonance imaging [20,21], and they have emerging uses in the fields of magnetic particle imaging [22] and cancer treatment [23]. They have been used *in vivo* for magnetomotive ultrasound imaging [24], and clustered magnetic nanoparticles have previously been used as a shear-wave source for transient elastography [25]. In a recently published paper, we showed that homogeneously distributed magnetic nanoparticles excited by a magnetic pulse can act as shear-wave sources in cell aggregates [26]. Assuming that dispersed magnetic microparticles excited by a pulsed magnetic field can act as shear-wave point sources, magnetic excitation of a magnetic hydrogel will lead to the instantaneous generation of a diffuse shear-wave field.

We present an experimental proof of concept for real-time magnetic elastography, which combines passive elastography imaging and a magnetomotive material made from dispersed magnetic microparticles. The instantaneous generation of a diffuse wave field allows us to shorten the correlation time needed to retrieve an elasticity contrast. We then show numerically that the imaging window can be shrunk to three time samples for an ideal source distribution. This is consistent with the theoretical minimum predicted by Gabor information theory.

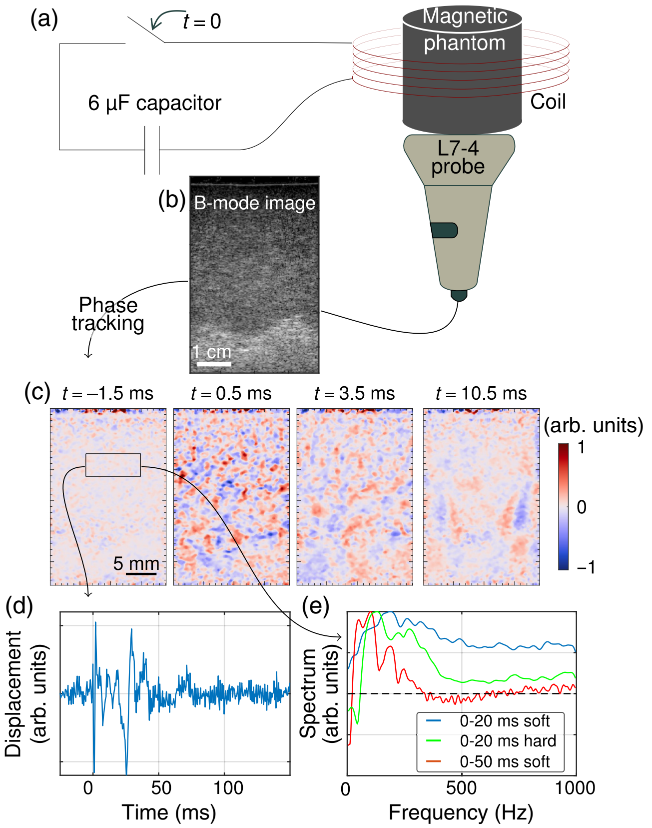

FIG. 1. Schematic experimental setup and imaging method. (a) A simplified electrical layout used to generate the magnetic pulse. (b) Example of an ultrasound backscatter (B-mode) image. (c) Exemplary snapshots of the axial particle velocity field at −1.5, 0.5, 3.5, and 10.5 ms, $t = 0$ being the start of the 0.2-ms magnetic pulse. (d) Spatially averaged time signal on the box depicted in (c). (e) Averaged spectral content of the wave fields for three different time windows, either in the soft (top) or stiff (bottom) layer (dashed black line: amplitude of −10 dB.

II. DIFFUSE-FIELD EXPERIMENT

A. Experimental setup

1. Fabrication of bilayered phantom

First, we created a bilayered elastic phantom consisting of gelatin powder (gelatin from porcine skin, G2500 Sigma-Aldrich, Burlington, MA, USA), xanthan gum (Meilleur du Chef, Bassussarry, France), and magnetic microparticles [Iron (II,III) oxide <5 μm, 310069, Sigma-Aldrich, Burlington, MA, USA]. The gelatin and xanthan powder were incorporated into warm water (90 °C), using concentrations of 0.25% xanthan (i.e., 0.25 g of xanthan per 100 mL solution), and 4 and 10% gelatin. Then, 1% microparticles were added, and the solution was mixed using a vibrating plate. The phantom was cooled down at 4 °C until complete gelation. To obtain a bilayered phantom of varying stiffness, the softer layer (4% gelatin) was first poured and gelled. In a second step, the other layer (10% gelatin) was poured on top of the first and gelled.

2. Magnetic-pulse excitation

As depicted in Fig. 1(a), the solidified gel was placed inside a coil connected to a home-made magnetic pulser [27]. The magnetic pulses were created by the discharge of a 6-μF capacitor, charged to 5 kV, through a 173-μH coil. This resulted in a 0.2-ms magnetic pulse of 250 mT in air. Note that the presence of paramagnetic particles leads to a higher field inside the sample. The gel was solidified without application of a magnetic field, and the magnetic particles should thus be distributed without a preferred orientation. Under the pulsed magnetic field, the magnetic particles will align along the magnetic field lines; as a result, a particle displacement or rotation is created on each individual microparticle. Because the magnetic particles are likely bound to the gelatin fibers by adhesive forces [28], the particle movement exerts a force on the elastic gel. Finally, each particle acts as an elastic-wave source of random directionality.

3. Ultrasound imaging

The bilayered sample was imaged using a clinical L7-4^{TM} (Philips ATL, Bothell, WA, USA) ultrasonic probe connected to a fully programmable ultrasound scanner (Verasonics Vantage^{TM}, Kirkland, WA, USA). The scanner and magnetic pulser were synchronized to retrieve the shear-wave field during and after the magnetic excitation.

Plane ultrasound waves were transmitted at three different angles from the 128-element array at a pulse-repetition frequency of 6000 Hz.

4. Noise-correlation shear-wave elastography

The compounding method [29] was applied to combine three low-quality images (one for each plane-wave angle) to obtain a single high-quality image [see Fig. 1(b)]. Overall, the frame rate was 2000 Hz. In addition, since an ultrasonic speckle is created by the magnetic microparticles, local motion can be tracked inside the phantom by measuring the displacement of the pattern that can be seen in Fig. 1(b). To this end, a phase-based motion estimator [30] was applied to the beam-formed IQ data of the backscattered US images to retrieve the axial particle velocity field u_z (vertical axis on the figures). Finally, a shear-wave speed map was retrieved using noise-correlation algorithms, based on a cross-correlation method applied to the shear-wave field [7,8,31,32]. Here, the local shear-wave speed is estimated as follows [32]:

$$c_s = \frac{\omega}{k} \cong \sqrt{\frac{1}{5}\frac{V^{\mathrm{TR}}}{\xi^{\mathrm{TR}}}} \text{ with } V^{\mathrm{TR}} = \frac{\partial u_z}{\partial t}(-t) \otimes \frac{\partial u_z}{\partial t}(t)$$

$$\text{and } \xi^{\mathrm{TR}} = \frac{\partial u_z}{\partial z}(-t) \otimes \frac{\partial u_z}{\partial z}(t), \quad (1)$$

where ω is the angular frequency, k the wave vector, z the spatial vertical coordinate, and t is the temporal coordinate. Here, TR indicates time reversal, and V^{TR} and ξ^{TR} are the time-reversed particle-velocity and strain fields. The algorithm temporally cross-correlates displacement signals between measurement points. At a time lag of zero, known as the refocusing time, the cross-correlation of one measurement point with all other points leads to a focal spot. The curvature of the focal spot at a given point is directly linked to the shear wavelength at this precise location [32]. It is worth mentioning that there is no spatial correlation mentioned here; both the central wavelength and period are estimated based on temporal cross-correlations between displacement signals. Initially, Eq. (1) was developed for diffuse wave fields detected in passive elastography; since then, it has been shown that noise-correlation elastography can also be applied to a nondiffuse wave field [33]. Although a nondiffuse wave field is not ideal for noise-correlation algorithms, longer correlation windows may be needed to accurately retrieve the local wavelength from the focal spot.

B. Toward real-time elastography: Retrieving an elasticity contrast in 20 ms

Snapshots of the acquired particle velocity field are displayed in Fig. 1(c), coded in red and blue, at four time points, before and after the magnetic excitation (beginning at $t = 0$ and ending at $t = 0.2$ ms). It can be seen that a nondirectional diffuse wave field was created by the pulsed magnetic field. This wave source is likely to also generate compressional waves, which propagate about 1000 times faster than shear waves in this quasi-incompressible medium; hence, they travel about 1 m between two frames and are rapidly attenuated. In addition, the amplitudes of compression waves in soft tissues are smaller than those of shear waves, which is why they are routinely ignored in ultrasound elastography. This is an assumption that we also make throughout this paper. The spatial average of the signal on a small region is plotted in Fig. 1(d); this contains high-frequency elastic waves with significant spectral content above 500 Hz, as shown in Fig. 1(e). The high frequencies are only detectable at early times due to rapid attenuation, as expected for viscoelastic solids; however, this strong attenuation due to the presence of high frequencies is not an issue because the sources are spread out everywhere in the imaged medium, and the medium is thus spatially covered with high-frequency wave propagation.

To retrieve the wave speed contrast, a noise-correlation algorithm was applied to the generated elastic wave field of Fig. 1. First, focal spots were calculated, and these are shown in Figs. 2(a) and 2(b). Figure 2(a) shows two focal spots at two points in the top and bottom layers, marked by black stars, calculated using a 100-time-step (50-ms) window. The wider focal spot in the bottom layer corresponds to a larger shear wavelength, which indicates a higher shear-wave velocity. This correlates with the bottom layer being stiffer than the top layer, as intended in the fabrication process. Figure 2(b) shows the same focal spots but for a 40-time-step (20-ms) window. The width difference between the two focal spots is conserved but with a lower signal-to-noise ratio.

Second, Figs. 2(c) and 2(d) show the shear-wave velocity maps retrieved using the noise-correlation algorithm summarized in Eq. (1). Figure 2(c) was obtained using the same 100 snapshots as above, and Fig. 2(d) was obtained using only 40 snapshots. Both wave velocity maps show a layering of the gel, and this is confirmed by the horizontally averaged wave velocity profiles plotted in Figs. 2(e) and 2(f). To confirm the elasticity layering of the phantom, we also performed an independent measurement using acoustic radiation force impulse shear-wave elastography (ARFI-SWE), the gold standard. The results are presented in the Appendix. The slower top layer (low gelatin concentration) is separated from the faster bottom layer (high gelatin concentration) at $\simeq$ 22 mm, which coincides with the interface depth found using ARFI-SWE. Hence, the analysis of a high-frequency wave field on 40 snapshots over 20 ms immediately after the magnetic pulse is sufficient to retrieve an elasticity contrast. Coupled to a fast data-processing algorithm, this type of experiment could allow the measurement of tissue elasticity in real time. We explicitly choose to present wave speed values and not

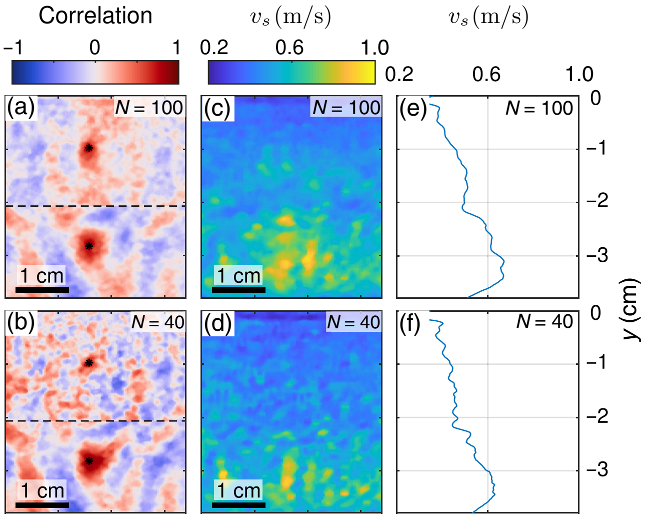

FIG. 2. Noise-correlation elastography results. Two focal spots calculated in each of the two elastic layers using (a) 100 snapshots (50 ms) and (b) 40 snapshots (20 ms) of displacements. Shear-wave speed maps retrieved using a noise-correlation elastography algorithm when considering (c) 100 and (d) 40 snapshots. (e),(f) Velocity profiles retrieved by averaging the speed maps shown in (c),(d) along the *x* axis.

shear moduli since wave speed is the data observable. Conversion to moduli would require an inversion through the application of a rheological model.

Quantitatively, the results for different correlation windows differ. The shortest window, which contains the highest-frequency content, results in a 20% (measured at 35-mm depth) higher speed profile than the longest window. Gelatin gels are strictly speaking not purely elastic but viscoelastic [34,35]; thus, the shear-wave speed increases with frequency. The shorter correlation window directly follows the magnetic impulse and exposes higher frequencies than later windows [see Fig. 1(c)]. The longer time window therefore gives more weight to the lower—and thus slower—frequencies. The effect only becomes clearly apparent in the stiffer (lower) part of the gel. We attribute this to an increased gelatin percentage in the lower gel, which likely results in a higher viscosity.

Using a magnetic stimulation impulse, we managed to retrieve a shear-wave velocity map by analyzing only 40 ms of acquisition. Nonetheless, the achievable temporal resolution in our magnetomotive experiment is limited by several factors: the access to a single component of the three-dimensional (3D) particle velocity field, the quantity and distribution of magnetic particles, and their adherence to the gelatin fibers. To test the minimum number of time samples needed to retrieve an elasticity contrast, we used a two-dimensional (2D) linear elastic simulation.

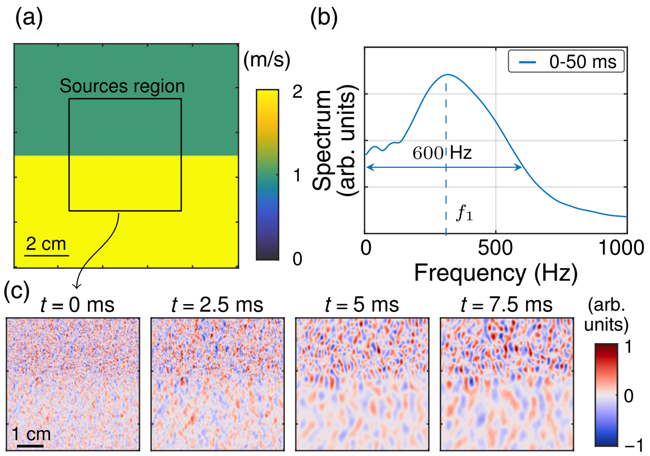

FIG. 3. Spectral-element simulation. (a) Shear-wave map of the bilayered medium. (b) Spectrum of the shear-wave field in the soft region. (c) Snapshots of the displacement field at four time points after the source excitation.

III. DIFFUSE-FIELD SIMULATION

A. Idealized 2D numerical experiment

We set up a 2D linear elastic spectral element simulation (Salvus package [36]) in a bilayered soft-tissue phantom. Both layers exhibit the same density (980 $\mathrm{kg\,m^{-3}}$) and compression wave speed (1500 $\mathrm{m\,s^{-1}}$), but a shear-wave speed contrast shown in Fig. 3(a): 1 $\mathrm{m\,s^{-1}}$ for the top layer and 2 $\mathrm{m\,s^{-1}}$ for the bottom layer. A total of 30 000 randomly polarized directional elastic point forces, required for exact Green's function retrieval [18], are randomly distributed in the region of interest (ROI) of the medium. They each generate a Ricker (Mexican-hat) pulse centered at 300 Hz. The boundary conditions are rigid on the edges of the medium, but boundary reflections do not reach the ROI during the simulation time. The elastic-wave propagation following the sources excitation is shown in Fig. 3(c) using four snapshots of the resulting particle velocity field. A diffuse displacement field containing waves propagating in all directions, without mode development, can be seen. The frequency content of this displacement is presented in Fig. 3(b). The spectrum aligns with the excitation and remains stable, confirming that the propagation is mode free.

B. Results

Two focal spots equivalent to Figs. 2(a) and 2(b) are presented in Figs. 4(a) and 4(b), using 100 and three time steps, respectively. The lower focal spot is larger than the upper one, revealing a larger shear wavelength and velocity for the bottom layer. Analyzing 100 snapshots with noise-correlation elastography [Eq. (1)], the wave speed map presented in Fig. 4(c) is obtained. It clearly shows a speed contrast between the two layers of the medium,

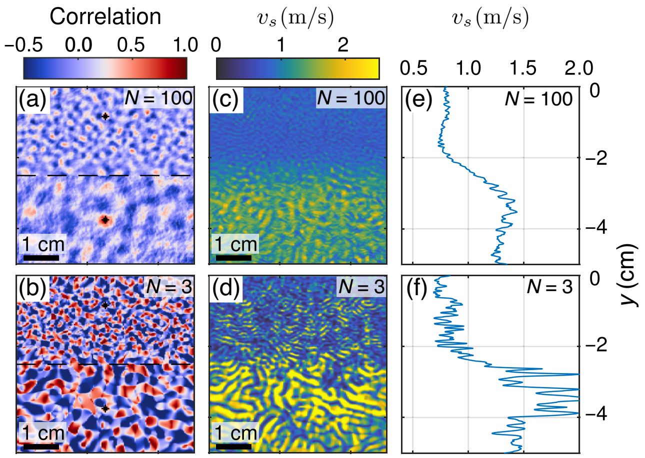

FIG. 4. Simulation: noise-correlation elastography results. Two focal spots calculated in each of the two layers retrieved using either (a) 100 or (b) three time points are merged together. Shear-wave speed maps retrieved through the correlation method, using either (c) 100 or (d) three displacement frames. (e),(f) Velocity profiles retrieved by averaging along the *x* axis of (c),(d).

again revealing a faster, stiffer medium in the bottom layer. The average wave speed profile along the depth in Fig. 4(e) displays a clear velocity step at the expected depth.

Since a diffuse wave field is the ideal case for noise-correlation algorithms, the minimum window length required can be investigated using this simulated dataset. The convolution in Eq. (1) leads to a secondary time derivative, and three time steps (frames) are therefore the minimal mathematical requirement of the algorithm. The results of noise correlation obtained using only three time steps are shown in Figs. 4(b), 4(d), and 4(f). In Fig. 4(d), the two layers are less homogeneous than in Fig. 4(c), but a clear wave velocity contrast is still retrieved. This is confirmed by the wave velocity profile shown in Fig. 4(f). The numerical simulation thus shows that numerous randomly distributed and orientated sources allow retrieval of a wave velocity contrast with the theoretical minimum number of time samples: three.

IV. DISCUSSION AND PERSPECTIVES

Our results show that a qualitative shear-wave speed mapping in real time is possible. Only 40 snapshots (20 ms) of the displacement field are required to achieve shear wave speed contrast imaging in our diffuse field experiment. Theoretically, under ideal conditions, the contrast of the bilayered phantom could be retrieved using only three snapshots, as shown in our numerical experiment. In the following, we discuss the conditions required to retrieve shear-wave speed contrast using a certain number of snapshots.

A. Link with Gabor's information theory

Since the correlation methods used in this paper are inspired by seismology [1–4,6], the temporal resolution of the method has rarely been investigated. Indeed, in seismology, the correlated time windows can extend up to one month; however, real-time modalities are essential in medical imaging since the medium can be changing quite fast, for example in the context of treatment monitoring. This is why the application of noise-correlation techniques to medical imaging leads to new questions such as the maximum achievable imaging frequency; however, it is well established that the longer the correlation window, the better the reconstructed wave speed map. According to Gabor's information theory [37–41], longer time windows capture more "information grains," where each grain represents a fundamental unit of information. Our two key questions for correlation applied to medical imaging are thus:

(1) How many information grains does an arbitrary correlation time window contain?

(2) What is the shortest time window that can be used for correlation?

The number of time-information grains N_T contained in a time window can be calculated through Gabor's uncertainty relation. This is the product of the frequency bandwidth and the window duration: $N_T = \Delta t \Delta f$ [37]. For a certain number of time-information grains, the contrast of the focal spot is given by $\gamma_{\text{corr}} = \sqrt{N_T}$, the contrast being defined as the ratio between the peak amplitude of the focal spot and its standard deviation. If the noise correlation that we use to retrieve focal spots and the wave speed maps obey Gabor's theory, then we have $\gamma_{\text{corr}}^2 = \Delta t \Delta f$.

In the magnetomotive experiment, a 20-ms time window having a $\simeq$1000-Hz bandwidth [blue curve of Fig. 1(d)] corresponds to 20 time-information grains. The focal-spot contrast of the soft layer in Fig. 2(b) is then $\gamma_{\text{corr}} = 5.15$, which leads to 26 measured time-information grains. The same calculations in the stiff region give a contrast of 3.7, corresponding to 13.6 time-information grains, which is in agreement with a shorter bandwidth [green curve of Fig. 1(d)]. Similarly, in the 2D elastic simulation, the correlation window lasting 50 ms, having a 600-Hz frequency bandwidth, contains 30 time-information grains, leading to a contrast of 5.7 [in the soft region of Fig. 4(a)]. Since $5.7^2 = 33$, the two values are compatible. Hence, there is very good agreement between the number of time-information grains theoretically contained in a certain correlation window and the resulting contrast for the focal spot. This is the first theoretical conclusion: the noise-correlation method obeys Gabor information theory, in that it manipulates time-information grains.

B. What is the shortest usable correlation window?

With the Gabor information approach validated, we now tackle the second key question: what is the shortest usable correlation window? For the central wavelength to be measurable at a certain spatial location, a focal spot has to be reconstructed. For this purpose, enough time-information grains must be contained in the correlation window to retrieve a local maximum at the chosen point. Hence, in one dimension, the standard deviation of a sinusoidal function being $1/\sqrt{2}$, the correlation contrast must be greater than $\sqrt{2}$. Similarly, we must have $\gamma_{\text{corr}} > \sqrt{2}^2 = 2$ in two dimensions and $\gamma_{\text{corr}} > \sqrt{2}^3 = 2\sqrt{2}$ in three dimensions. Since $\gamma_{\text{corr}}^2 = \Delta t \Delta f$, for a certain frequency bandwidth, the shortest correlation window allowing the calculation of a focal spot is given by

$$\begin{cases} \Delta t > \frac{\sqrt{2}^2}{\Delta f} = \frac{2}{\Delta f} \text{ in one dimension,} \\ \Delta t > \frac{2^2}{\Delta f} = \frac{4}{\Delta f} \text{ in two dimensions,} \\ \Delta t > \frac{(2\sqrt{2})^2}{\Delta f} = \frac{8}{\Delta f} \text{ in three dimensions.} \end{cases}$$

Therefore, in the 2D elastic simulation previously presented, the frequency bandwidth being around 600 Hz, the shortest correlation window that can be used to retrieve a focal spot at all points is $\Delta t = (4/\Delta f) = (4/600) = 6.6$ ms, which corresponds to a frame rate of 150 Hz. Hence, the three-time-step correlation window is even shorter (3 ms) than the theoretical shortest time. Indeed, in Fig. 4(d), it can be seen that the exact wave speed is not well retrieved at all points since a focal spot cannot be retrieved for all points. In the end, when averaging along the image width [Fig. 4(f)], the speed contrast as a function of depth is conserved, but quantitative wave speed imaging is barely possible.

C. Perspectives: Implications for real-time imaging and monitoring

In clinically used methods such as ARFI imaging combined with time-of-flight techniques, a minimum acquisition time corresponding to a minimum wavefront propagation length are required to estimate the shear-wave speed. If a magnetomotive elastography method were to be used in combination with noise-correlation algorithms, only a few time steps could be used to detect elasticity contrast. Indeed, magnetic nanoparticles are already widely used *in vivo* as contrast agents in magnetic resonance imaging [20,21], are emerging in the field of magnetic particle imaging [22], and they have been used for magnetomotive ultrasound imaging [24,42,43]. Hence, our experiment shows that the clinical use of real-time magnetomotive elastography is realistic and could unlock real-time elasticity estimation.

V. CONCLUSION

To conclude, we experimentally realized diffuse elastic fields *in situ* through the combination of a magnetic pulser and magnetic particles. Our 3D laboratory realization, 2D numerical experiments, and theoretical considerations show that only a few discrete time steps are required to retrieve an elasticity contrasts using noise correlation under ideal conditions. A direct imaging application is elasticity characterization in the medical field. Our proof-of-concept experiment suggests that cross-correlation imaging in real time, as demanded by physicians, is becoming feasible. The same nanoparticles that are already used for cancer treatment and magnetic resonance imaging have the potential to create diffuse wave fields for real-time treatment monitoring.

In principle, our findings are applicable to any wavefield correlation method that uses a dense array of receivers to image medium contrasts, such as distributed acoustic sensing, digital image correlation, dense array seismology, or nondestructive testing.

ACKNOWLEDGMENTS

This project has received funding from the Plan Cancer ARC-2018-PhysiCancer-BPALP, the Swiss National Foundation under Grant No. 197182, and with financial support from ITMO Cancer of Aviesan within the framework of the 2021–2030 Cancer Control Strategy, on funds administered by Inserm.

APPENDIX: COMPARISON WITH A GOLD STANDARD: ACOUSTIC RADIATION FORCE IMPULSE-SHEAR WAVE ELASTOGRAPHY

As a ground-truth elasticity measurement, we implemented ARFI-SWE in the phantom of Fig. 1. In ARFI-SWE, the focusing of ultrasonic waves at a point in the medium of interest creates a force, which in turn acts as a shear-wave source. Immediately after the shear-wave generation, the same plane-wave imaging sequence as in the diffuse-field experiment was used. Then, the shear-wave field was retrieved using the same phase-based motion estimator. The three exemplary displacement snapshots in Fig. 5(a) show a shear-wave front originating from the focusing of ultrasonic beams at a depth of 25 mm and in the lateral center of the probe. It can already be seen that the wave front propagates faster in the bottom layer than in the top layer. Next, we applied Eq. (1) to the ARFI-SWE displacements. The resulting shear-wave velocity map displayed in Fig. 5(b) shows a clear velocity contrast between the two layers, except on the wave source location (central vertical line). Finally, a classical time-of-flight algorithm [44] was used for comparison. In Fig. 5(c) the velocity profiles are plotted as a function of depth, obtained using either

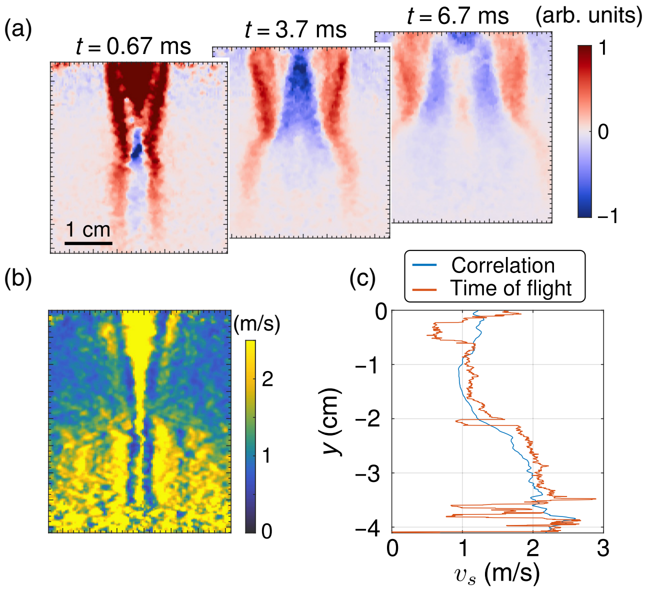

FIG. 5. Ultrasonic push (ARFI) results. (a) Snapshots of the displacement film at three times. (b) Shear-wave velocity map retrieved using passive elastography algorithms. (c) Velocity profiles as a function of depth retrieved by averaging the shear-wave velocity map in (b) and measuring the time of flight.

noise-correlation or time-of-flight approaches. Both algorithms retrieve a sharp velocity increase at 22 mm depth, in accordance with Fig. 2. The profile obtained using correlation is smoother than the time-of-flight profile, but they quantitatively agree (rms $\simeq 0.15\ \mathrm{m\,s^{-1}}$). This corroborates the measurements showing the different elasticities of the bilayered gel phantom; however, the shear-wave speeds differ from the previous results. This may be due to either the difference in the frequency content leading to dispersion in viscoelastic media or the presence of measurement noise. This noise may impact the focal spot when noise-correlation approaches are performed in other sections. This phenomenon can be observed in seismology [45].

[1] D. Ayala-Garcia, A. Curtis, and M. Branicki, Seismic interferometry from correlated noise sources, Remote Sens. (Basel) **13**, 2703 (2021).

[2] D.-J. van Manen, J. O. A. Robertsson, and A. Curtis, Modeling of wave propagation in inhomogeneous media, Phys. Rev. Lett. **94**, 164301 (2005).

[3] M. Campillo and A. Paul, Long range correlations in the diffuse seismic coda, Science **299**, 547 (2003).

[4] A. Sergeant, M. Chmiel, F. Lindner, F. Walter, P. Roux, J. Chaput, F. Gimbert, and A. Mordret, On the Green's function emergence from interferometry of seismic wave fields generated in high-melt glaciers: Implications for passive imaging and monitoring, The Cryosphere **14**, 1139 (2020).

[5] J. Spytek, L. Pieczonka, T. Stepinski, and L. Ambrozinski, Mean local frequency-wavenumber estimation through synthetic time-reversal of diffuse Lamb waves, Mech. Syst. Signal Process **156**, 107712 (2021).

[6] L. Eisner, P. M. Duncan, W. M. Heigl, and W. R. Keller, Uncertainties in passive seismic monitoring, Lead. Edge **28**, 648 (2009).

[7] T. Gallot, S. Catheline, P. Roux, J. Brum, N. Benech, and C. Negreira, Passive elastography: Shear-wave tomography from physiological-noise correlation in soft tissues, IEEE Trans. Ultrason. Ferroelectr. Freq. Control **58**, 1122 (2011).

[8] S. Catheline, R. Souchon, M. Rupin, J. Brum, A. H. Dinh, and J. Y. Chapelon, Tomography from diffuse waves: Passive shear wave imaging using low frame rate scanners, Appl. Phys. Lett. **103**, 014101 (2013).

[9] A. Zorgani, R. Souchon, A.-H. Dinh, J.-Y. Chapelon, J.-M. Ménager, S. Lounis, O. Rouvière, and S. Catheline, Brain palpation from physiological vibrations using MRI, Proc. Natl. Acad. Sci. USA **112**, 12917 (2015).

[10] T.-M. Nguyen, A. Zorgani, M. Lescanne, C. Boccara, M. Fink, and S. Catheline, Diffuse shear wave imaging: Toward passive elastography using low-frame rate spectral-domain optical coherence tomography, J. Biomed. Opt. **21**, 126013 (2016).

[11] P. Grasland-Mongrain, A. Zorgani, S. Nakagawa, S. Bernard, L. G. Paim, G. Fitzharris, S. Catheline, and G. Cloutier, Ultrafast imaging of cell elasticity with optical microelastography, Proc. Natl. Acad. Sci. USA **115**, 861 (2018).

[12] J. Brum, N. Benech, T. Gallot, and C. Negreira, Shear wave elastography based on noise correlation and time reversal, Front. Phys. **9**, 617445 (2021).

[13] A. Derode, P. Roux, and M. Fink, Robust acoustic time reversal with high-order multiple scattering, Phys. Rev. Lett. **75**, 4206 (1995).

[14] J. F. Claerbout, Synthesis of a layered medium from its acoustic transmission response, Geophysics **33**, 264 (1968).

[15] R. L. Weaver, On diffuse waves in solid media, J. Acoust. Soc. Am. **71**, 1608 (1982).

[16] R. L. Weaver and O. I. Lobkis, Ultrasonics without a source: Thermal fluctuation correlations at MHz frequencies, Phys. Rev. Lett. **87**, 1 (2001).

[17] A. Hejazi Nooghabi, L. Boschi, P. Roux, and J. de Rosny, Coda reconstruction from cross-correlation of a diffuse field on thin elastic plates, Phys. Rev. E **96**, 032137 (2017).

[18] K. Wapenaar, J. Fokkema, and R. Snieder, Retrieving the Green's function in an open system by cross correlation: A comparison of approaches, J. Acoust. Soc. Am. **118**, 2783 (2005).

[19] A. C. Prunty, R. K. Snieder, and C. Sens-Schönfelder, Acoustic imaging using unknown random sources, J. Acoust. Soc. Am. **149**, 499 (2021).

[20] S. Mornet, S. Vasseur, F. Grasset, P. Veverka, G. Goglio, A. Demourgues, J. Portier, E. Pollert, and E. Duguet, Magnetic nanoparticle design for medical applications, Prog. Solid State Chem. **34**, 237 (2006).

[21] C. Fang and M. Zhang, Multifunctional magnetic nanoparticles for medical imaging applications, J. Mater. Chem. **19**, 6258 (2009).

[22] J. Borgert, J. D. Schmidt, I. Schmale, J. Rahmer, C. Bontus, B. Gleich, B. David, R. Eckart, O. Woywode, J. Weizenecker, J. Schnorr, M. Taupitz, J. Haegele, F. M. Vogt, and J. Barkhausen, Fundamentals and applications of magnetic

particle imaging, J. Cardiovasc. Comput. Tomogr. **6**, 149 (2012).

[23] A. Farzin, S. A. Etesami, J. Quint, A. Memic, and A. Tamayol, Magnetic nanoparticles in cancer therapy and diagnosis, Adv. Healthc. Mater. **9**, e1901058 (2020).

[24] M. Mehrmohammadi, T.-H. Shin, M. Qu, P. Kruizinga, R. L. Truby, J.-H. Lee, J. Cheon, and S. Y. Emelianov, In vivo pulsed magneto-motive ultrasound imaging using high-performance magnetoactive contrast nanoagents, Nanoscale **5**, 11179 (2013).

[25] T. Z. Pavan, D. R. T. Sampaio, A. A. O. Carneiro, and D. T. Covas, in *2012 IEEE International Ultrasonics Symposium* (Dresden, Germany, 2012), pp. 1846–1849.

[26] G. Laloy-Borgna, L. Vovard, A. Rohfritsch, L. Wang, J. Ngo, M. Perier, A. Drainville, F. Prat, M. Lafond, C. Lafon, and S. Catheline, Magnetic microelastography for evaluation of ultrasound-induced softening of pancreatic cancer spheroids, Phys. Rev. Appl. **22**, 024024 (2024).

[27] Z. Sun, B. Giammarinaro, A. Birer, G. Liu, and S. Catheline, Shear wave generation by remotely stimulating aluminum patches with a transient magnetic field and its preliminary application in elastography, IEEE Trans. Biomed. Eng. **68**, 2129 (2021).

[28] J. R. Morillas and J. de Vicente, Magnetorheology: A review, Soft Matter **16**, 9614 (2020).

[29] M. Tanter and M. Fink, Ultrafast imaging in biomedical ultrasound, IEEE Trans. Ultrason. Ferroelectr. Freq. Control **61**, 102 (2014).

[30] G. Pinton, J. Dahl, and G. Trahey, in *IEEE Ultrasonics Symposium, 2005*, Vol. 4 (IEEE, Rotterdam, Netherlands, 2005), p. 2062.

[31] N. Benech, J. Brum, S. Catheline, T. Gallot, and C. Negreira, Near-field effects in Green's function retrieval from cross-correlation of elastic fields: Experimental study with application to elastography, J. Acoust. Soc. Am. **133**, 2755 (2013).

[32] C. Zemzemi, A. Zorgani, L. Daunizeau, S. Belabhar, R. Souchon, and S. Catheline, Super-resolution limit of shear-wave elastography, Europhys. Lett. **129**, 34002 (2020).

[33] A. Marmin, S. Catheline, and A. Nahas, Full-field passive elastography using digital holography, Opt. Lett. **45**, 2965 (2020).

[34] G. Laloy-Borgna, A. Zorgani, and S. Catheline, Micro-elastography: Toward ultrasonic shear waves in soft solids, Appl. Phys. Lett. **118**, 113701 (2021).

[35] S. Catheline, J. L. Gennisson, G. Delon, M. Fink, R. Sinkus, S. Abouelkaram, and J. Culioli, Measuring of viscoelastic properties of homogeneous soft solid using transient elastography: An inverse problem approach, J. Acoust. Soc. Am. **116**, 3734 (2004).

[36] M. Afanasiev, C. Boehm, M. van Driel, L. Krischer, M. Rietmann, D. A. May, M. G. Knepley, and A. Fichtner, Modular and flexible spectral-element waveform modelling in two and three dimensions, Geophys. J. Int. **216**, 1675 (2019).

[37] D. Gabor, Theory of communication. Part 1: The analysis of information, J. Inst. Electr. Eng. - Part III: Radio Commun. Eng. **93**, 429 (1946).

[38] D. Gabor, Communication theory and physics, Trans. IRE Professional Group Inf. Theory **1**, 48 (1953).

[39] D. Gabor, The transmission of information by coherent light. I. Classical theory, J. Phys. E: Sci. Instrum. **8**, 73 (1975).

[40] D. Gabor, in *Progress in Optics*, Vol. 1, edited by E. Wolf (Elsevier, Amsterdam, 1961), p. 109.

[41] M. Franceschetti, *Wave Theory of Information* (Cambridge University Press, Cambridge, 2017).

[42] J. Oh, M. D. Feldman, J. Kim, C. Condit, S. Emelianov, and T. E. Milner, Detection of magnetic nanoparticles in tissue using magneto-motive ultrasound, Nanotechnology **17**, 4183 (2006).

[43] Y. Hadaian, D. R. T. Sampaio, A. P. Ramos, A. A. O. Carneiro, and T. Z. Pavan, in *2017 IEEE International Ultrasonics Symposium (IUS)* (Washington, DC, USA, 2017), pp. 1–4.

[44] J.-L. Gennisson, T. Deffieux, M. Fink, and M. Tanter, Ultrasound elastography: Principles and techniques, Diagn. Interv. Imaging **94**, 487 (2013).

[45] B. Giammarinaro, C. Tsarsitalidou, G. Hillers, J. de Rosny, L. Seydoux, S. Catheline, M. Campillo, and P. Roux, Seismic surface wave focal spot imaging: Numerical resolution experiments, Geophys. J. Int. **232**, 201 (2023).